PCCP
Physical Chemistry Chemical Physics

Accepted Manuscript

This article can be cited before page numbers have been issued, to do this please use: N. Latas, D. Pjevic, J. P. Georgijevi, D. Jugovi, S. Stojadinovic and N. Cvjeticanin, *Phys. Chem. Chem. Phys.*, 2025, DOI: 10.1039/D5CP01788B.

View Article Online
DOI: 10.1039/D5CP01788B

Surface engineering of TiO_2 nanotubes with tantalum for improved electrochemical performance

Nemanja Latas[1#], Dejan Pjević[1*], Jelena P. Georgijević[1], Dragana Jugović[2], Stevan Stojadinović[3], Nikola Cvjetićanin[4]

[1]*Department of Atomic Physics, INS Vinča – National Institute of the Republic of Serbia, University of Belgrade, Mike Petrovića Alasa 12-14, Belgrade, Serbia*

[2]*Institute of Technical Sciences of SASA, Kneza Mihaila 35/IV, Belgrade, Serbia*

[3]*Faculty of Physics, University of Belgrade, Studentski trg 12-16, Belgrade, Serbia*

[4]*University of Belgrade – Faculty of Physical Chemistry, Studentski trg 12-16, Belgrade, Serbia*

Abstract: In this work, TiO_2 anatase nanotubes (NTs) were synthesized using a straightforward, two-step anodic oxidation method. To tackle with the optical and electrical properties of the material, a thin layer of tantalum was sputtered onto the nanotube surface. The microstructure of the modified material was analyzed using scanning and transmission electron microscopy (SEM and TEM), while changes in chemical bonding were examined by utilizing X-ray photoelectron spectroscopy (XPS). Structural analysis found the formation of β-Ta_2O_5 phase on the surface of deposited TiO_2 NTs. Electrical resistivity, measured with the 4-point probe technique, showed a reduction in resistivity for the modified material, implying an increase in conductivity. Diffuse reflectance spectroscopy (DRS) showed an increase in the energy gap from 3.05 eV to 3.85 eV, while photoluminescence (PL) spectra revealed a suppression of deep-level trap states within the

#Current address: National Institute of Chemistry, Hajdrihova 19, 1000, Ljubljana, Slovenia.

*Corresponding author: Dr Dejan Pjević, INS "Vinča", National Institute of the Republic of Serbia, University of Belgrade, Mike Petrovića Alasa 12-14, Belgrade, Serbia. Email: dejanp@vin.bg.ac.rs.

View Article Online
DOI: 10.1039/D5CP01788B

bandgap for modified NTs. These results indicate that increased conductivity can most probably be attributed to the reduction of Ti^{4+} to Ti^{3+}, modification of surface oxygen states and suppression of deep-level trap states within the bandgap for Ta deposited nanotubes. Electrochemical tests further revealed improved capacity for Li-ion intercalation, as well as Coulombic efficiency, particularly at elevated temperatures.

1. Introduction

Research into the use of semiconductor materials in electrochemical systems has gained significant attention for a variety of energy storage and conversion devices. The incorporation of semiconductors into electrochemistry has transformed the field, advanced our understanding of interfacial reactions and bridged gaps between electrochemistry, solid-state physics, and photochemistry. This integration has opened new avenues for research and applications.[1] This rapidly growing field highlights the advantages of semiconducting materials over traditional counterparts, offering not only enhancements in specific properties but also the introduction of entirely new behaviors. The unique functional properties of semiconductors, such as tunable electronic structures, defect engineering, mixed ionic-electronic conductivity, distinguishes them from conventional materials and make them particularly well-suited for advanced applications in electrochemical devices.[2,3] Although semiconductor materials can exhibit unique properties, nanostructuring is often necessary to fully leverage their potential for advanced applications.[4] Unlike bulk materials, nanostructures can overcome limitations such as low conductivity and poor stability while enabling tunable electrical, optical, and catalytic properties. Advances in band

View Article Online
DOI: 10.1039/D5CP01788B

engineering have solidified their role in driving innovation in energy conversion, storage, and catalysis.[5] In particular, the improvement of semiconductor materials through various modification strategies has been extensively explored.[6]

TiO_2 is one of the most extensively studied semiconductor materials, attracting significant interest for applications in solar cells, photocatalysis, sensors, and biomedical technologies.[7] Among these, nanostructured TiO_2 has gained attention as a promising anode material for Li-ion batteries due to its ability to enhance energy storage, reduce charging time, and extend battery lifespan through structural, porosity, phase, and conductivity optimizations.[8] Its wide applicability stems from properties that can be tailored through morphology control and impurity incorporation. These modifications enable the optimization of its electronic properties, further enhancing its performance in various applications.[9]

Strategies for enhancing the performance of TiO_2-based materials include hetero-atom doping, which can involve the incorporation of non-metal elements such as N[10,11], F[12], B[13] and P[14] as well as metal dopants, including Cu[15], Fe, Mn, Co[16] and Ni[17], among others. Usui et al[18] demonstrated improved properties of the rutile TiO_2 structure through doping with Ta, Nb, Sn, and In using hydrothermal synthesis. Among all metal dopants, Ta exhibited the most significant enhancement in charge storage properties for Na-ion batteries. Another widely explored strategy is the formation of TiO_2-carbon nanocomposites[19-21], to enhance electrical conductivity and ion diffusion while also improving the dispersion of TiO_2 nanoparticles, increasing the number of active sites for Li^+ storage. However, the stability of some carbon materials at high temperatures can be a drawback, particularly for highly porous carbon materials, which may degrade or react with the electrolyte under extreme conditions[22].

View Article Online
DOI: 10.1039/D5CP01788B

Another promising strategy for modifying TiO_2 is defect engineering, as defects can have a significant impact on its electrical properties. For example, oxygen vacancies can enhance the material's conductivity by increasing the number of free electrons. This occurs because oxygen vacancies act as electron donors, leading to the formation of Ti^{3+} states that contribute to improved charge transport[23]. Previous studies explored the influence of material defects on the performance of Li-ion batteries[24,25]. Zhang et al[26] highlighted the importance of defect engineering in design of electrode materials, as the introduction of defects into the crystal structure can enhance conductivity and capacity. This, in turn, improves the reversibility of the insertion/extraction reaction, leading to higher Coulombic efficiency. The way to further enhance the performance of such systems include the formation of heterostructures between TiO_2 and other metal oxides, which have been shown to improve charge transport and cycling stability for Li-ion battery applications[27]. Several studies have reported modifications of TiO_2 with various metal oxides, including SnO_2[28], Fe_2O_3[29], and Sb_2O_3[30]. Lee et al[31] prepared TiO_2/SiO_2 nanocomposite films with high capacitance and good stability using the plasma electrolytic oxidation method, which enables the formation of porous oxide materials.

In this study, we explore the microstructural, electrical, and optical properties of TiO_2 nanotubes (NTs) modified through direct current sputtering of tantalum. The focus of this work was on understanding the relationship between the sputtering process and the resulting modifications in the optical bandgap, alongside the creation of distinct defect states within the material. To further assess the performance of such material as a potential anode material in Li-ion batteries, it was subject to electrochemical testing at both room and elevated temperatures (up to 55°).

View Article Online
DOI: 10.1039/D5CP01788B

2. Experimental

Material preparation – Nanostructured anatase TiO_2 NTs were synthesized using a straightforward two-step anodic oxidation method. A piece of titanium foil (Wiliam Gregor $\omega \geq 0.995$) was first polished with sandpaper, then degreased in acetone (Lach-Ner, 99.99%) for 15 minutes, followed by 15 minutes in isopropyl alcohol (J. T. Baker, ≥ 99.5%). The polished foil was immersed in a 0.7 wt% NH_4F (Kemika-Zagreb, p.a.) solution in glycerol (Zorka Šabac, 86-88%), and a potential of 45 V was applied against a graphite cathode for 4 hours, resulting in the formation of amorphous TiO_2 nanotubes. The electrode was then annealed for 3 hours at 400°C to produce the anatase phase and will henceforth be referred to as the Ti/TiO_2 nanotube arrays (NTAs) electrode. This electrode was analyzed for its microstructural and electrochemical properties, and was used as a substrate for tantalum (Ta) film deposition in a Balzers Sputtron II system, utilizing a Ta target (Balzers, 99.99%) with DC ion sputtering. The resulting electrode will be designated as $Ti/TiO_2/Ta$ NTAs electrode in the following text. Additionally, silicon wafers (100) were used as a reference for determination of film thickness. The base pressure prior to deposition was $6 \cdot 10^{-4}$ Pa, while the partial pressure of argon, used as the sputtering gas, was set to at $1 \cdot 10^{-1}$ Pa. The deposition times were limited to 100, 160, and 220 seconds. However, electrochemical measurements indicated that 160 s was the optimal deposition time (details provided in the Supplementary Material) based on Coulombic efficiency and specific capacity values. Therefore, all experiments were conducted using materials with Ta deposition time of 160 s.

View Article Online
DOI: 10.1039/D5CP01788B

Material characterization – The X-ray diffraction (XRD) patterns of the Ti/TiO_2 and $Ti/TiO_2/Ta$ NTAs electrodes were obtained using a Philips PW 1050 diffractometer with Cu-$K\alpha_{1,2}$ radiation, scanning a 2θ range of 20-80° with a step size of 0.05° and a counting time of 3 seconds per step. The morphology of the samples was analyzed using a FEI SCIOS 2 Dual Beam field emission scanning electron microscope (FE-SEM). Additionally, transmission electron microscopy (TEM) analysis was performed in cross-sectional view, with electron-transparent lamellas prepared using a focused ion beam (FIB) in an FEI Scios 2 Dual Beam system. The examination was conducted using a FEI Talos F200X TEM equipped with an energy dispersive X-ray spectroscopy (EDX) system. Alongside conventional TEM studies, high-angle annular dark-field imaging (HAADF) in scanning transmission electron microscopy (STEM) mode and selected area electron diffraction (SAED) were also conducted to gain insights into the structure of the NTAs.

Chemical analysis of the samples was conducted using X-ray photoelectron spectroscopy (XPS) with a SPECS System featuring an XP50M X-ray source for the Focus 500 and a PHOIBIOS 100/150 analyzer. The spectra were excited using monochromatic Al Kα radiation (1486.7 eV). Survey spectra were recorded with a constant pass energy of 50 eV, a step size of 0.5 eV, and a dwell time of 0.2 seconds in fixed analyzer transmission (FAT) mode. High-resolution spectra of the Ti 2p, O 1s, and C 1s peaks were obtained with a constant pass energy of 20 eV, a step size of 0.05 eV, and a dwell time of 0.2 seconds in FAT mode. The base pressure of the instrument during the experiments was approximately $1 \cdot 10^{-9}$ mbar. To minimize the charging effects on the samples, an electron flood gun (SPECS FG15/40) was employed for charge

View Article Online
DOI: 10.1039/D5CP01788B

neutralization, and all peak positions were referenced to the C 1s peak at 285.0 eV. The data was analyzed using the CasaXPS software package.

Diffuse reflectance UV-Vis spectroscopy (DRS) measurements were carried out using a UV-2600I spectrophotometer with integrating sphere (Shimadzu). DRS spectra were acquired in the spectral range of 200-800 nm, with a scanning speed of 300 nm/min. Photoluminescence spectral measurements were performed on a Horiba Jobin Yvon Fluorolog FL3-22 spectrofluorometer at room temperature, with a 450 W Xe-lamp as the excitation light source. Excitation energy used for all samples was set at 380 nm. All obtained spectra were corrected for the spectral response of the measuring system and spectral distribution of the Xe-lamp. Resistivity of the samples was determined by the four-point probe method, using Jaden Universal Probe-model 3000 RM in a linear configuration.

Electrochemical measurements – all electrochemical experiments were carried out in a bottle-like two-electrode cell, made from Pyrex glass, with electrical contacts routed through a Teflon stopper with a double ″O″ ring. Prepared materials were used as working electrodes, while a piece of Li-foil was used as the counter electrode. The cell was filled with about 4 cm^3 of electrolyte, 1 M $LiClO_4$ in propylene carbonate. Galvanostatic (GS) cycling experiments were conducted using Arbin BT 2042 battery testing device. The electrochemical impedance spectroscopy (EIS) measurements were performed on Gamry 1010E Potentiostat/Galvanostat in the frequency range from 100 kHz to 0.01 Hz. Experiments were carried out using a HAAKE F3 thermostat.

3. Results & discussion

View Article Online
DOI: 10.1039/D5CP01788B

Microstructural characterization of the prepared samples – The XRD patterns in Figure 1 for the Ti/TiO_2 and $Ti/TiO_2/Ta$ NTAs electrodes were recorded to examine the impact of tantalum sputtering.

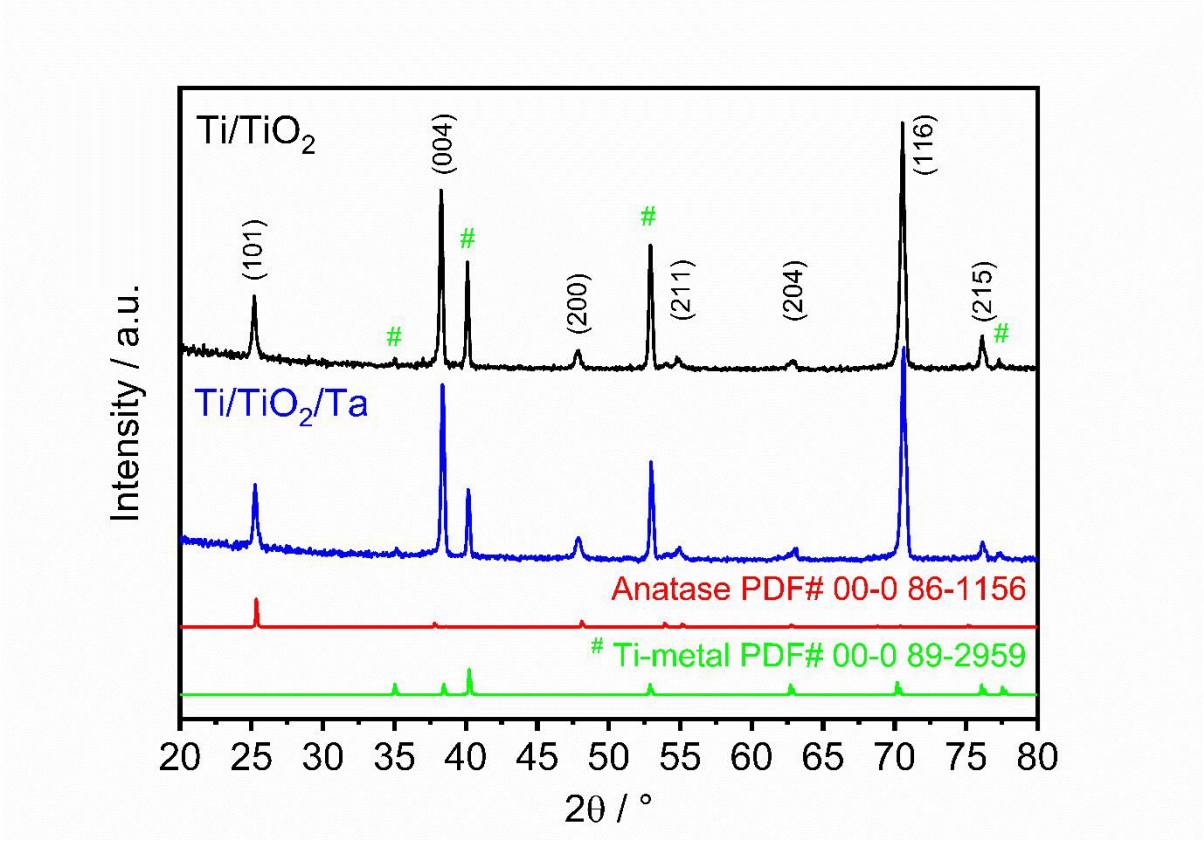

Figure 1. XRD patterns of Ti/TiO_2 and $Ti/TiO_2/Ta$ NTAs electrodes.

The patterns contain only peaks belonging to the anatase and titanium phases with no additional peaks after tantalum sputtering. After sputtering, the peaks are slightly shifted, and their half-width are changed, implying changes in both lattice parameters and crystallite size. Interestingly, after sputtering, the peak intensities decrease only for pure titanium. The strongest individual peaks of anatase and titanium (at around 25° and 40°, respectively) were used for

View Article Online
DOI: 10.1039/D5CP01788B

calculating the mean crystallite size, employing the XFIT software with a Fundamental Parameters convolution approach to generate line profiles.[32] The Le Bail whole pattern decomposition method[33] was used to calculate the lattice parameters. Two-phase refinement was performed in the tetragonal I41/amd and the hexagonal P63/mmc space groups, for TiO_2 and Ti, respectively. The calculated lattice parameters of the two phases of both electrodes are in agreement with the literature data (PDF# 00-089-2762 for TiO_2 and PDF# 00-086-1156 for Ti). The results of the fittings are presented in Table 1.

Table 1. The mean crystallite sizes and lattice parameters obtained from XRD analysis.

Phase	Electrode	Spece group	*a* / Å	*b* / Å	*c* / Å	Crystallite size / nm
TiO_2	Ti/TiO_2	I41/amd	2.94947	2.94947	4.69059	32
	Ti/TiO_2/Ta		2.95237	2.95237	4.49275	34
Ta	Ti/TiO_2	P63/mmc	3.79382	3.79382	9.45364	57
	Ti/TiO_2/Ta		3.80076	3.80076	9.46383	54

After tantalum spattering, lattice parameters increase for both phases, accompanied by an increase in TiO_2 crystallites and a decrease in Ti crystallites. Lattice expansion can be associated with the incorporation of larger tantalum into the lattice, which causes additional lattice strain due to both the larger tantalum radius and its valence. Specifically, in the case of TiO_2, the incorporation of Ta(V) causes oxygen vacancies through the reduction of Ti(IV) to Ti(III), initiating additional strain and expansion of the lattice. These finding are consistent with TEM and

View Article Online
DOI: 10.1039/D5CP01788B

XPS results. Smaller crystallites of titanium, along with smaller peak intensities, imply dissolution of titanium for the formation of TiO_2 NTs.

To gain a deeper understanding of the microstructure of the systems under investigation, the samples were analyzed using scanning and transmission electron microscopy. The plain-view FE-SEM images and the results of the microstructural TEM analysis are displayed in Figure 2 (a-b) and Figure 3 (a-f), respectively.

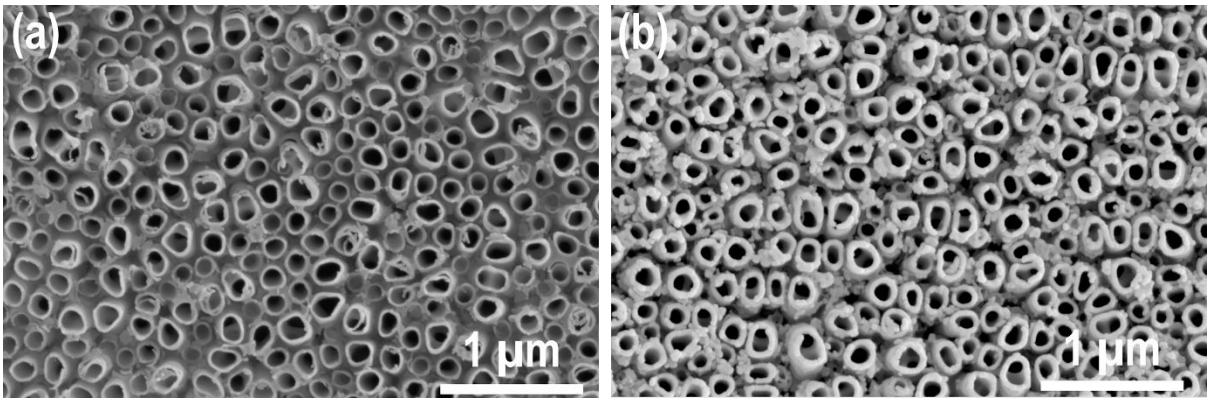

Figure 2. Plain-view FE-SEM micrographs: Ti/TiO_2 (a) and Ti/TiO_2/Ta NTAs (b) electrodes.

The plain-view FE-SEM micrographs in Figure 2 (a) and (b) clearly show that both samples consist of cylindrical, well-separated NTs. The average inner diameter of the NTs is approximately 125 nm for the Ti/TiO_2 electrode and about 108 nm for the Ti/TiO_2/Ta electrode. Furthermore, the average wall thickness of the nanotubes increased from around 25 nm to approximately 40 nm after tantalum deposition. Notably, the deposited Ta layer does not ''fuse'' the nanotubes together, but significantly reduces the space between them.

View Article Online
DOI: 10.1039/D5CP01788B

Low-magnification bright-field TEM micrographs of Ti/TiO_2 and $Ti/TiO_2/Ta$ NTAs electrodes presented in Figures 3 (a) and (b), respectively, reveal the overall structure of the samples.

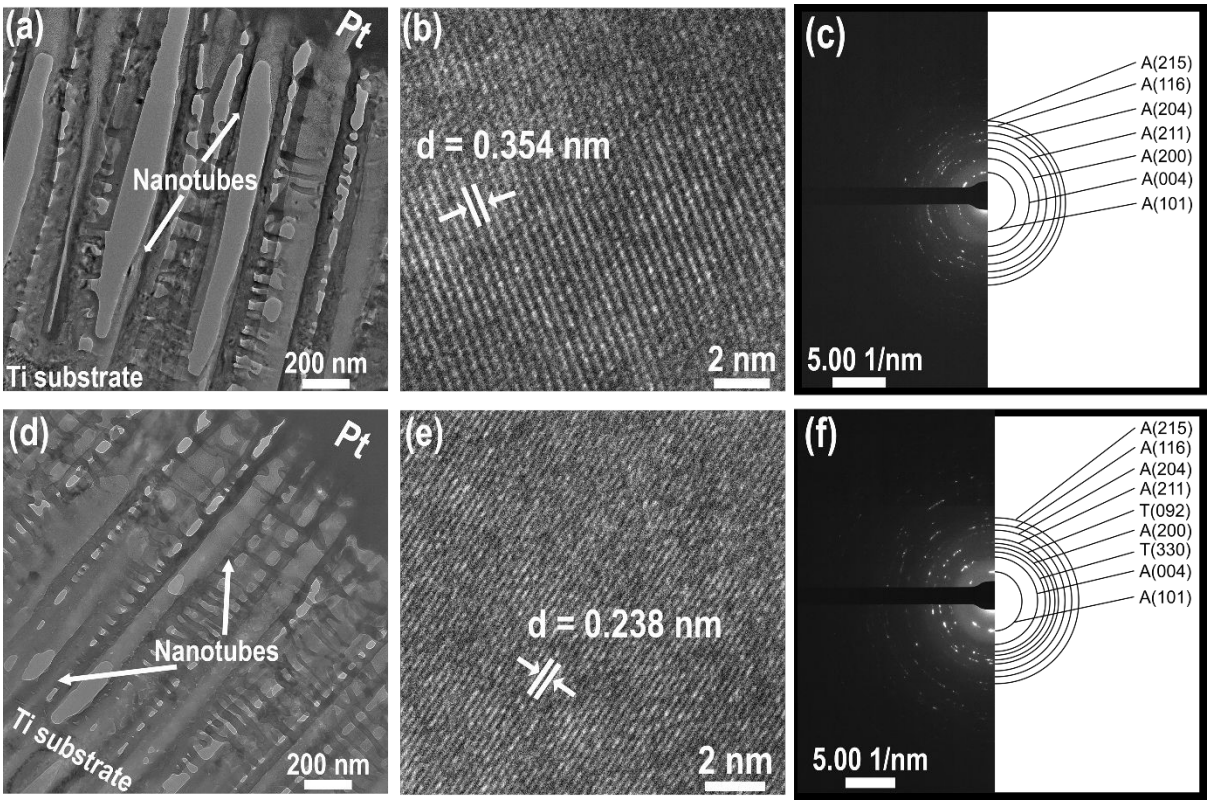

Figure 3. TEM analysis of the samples: bright-field micrographs (a,d); HR-TEM images (b,e); and SAED diffraction patterns (c,f) for the as-prepared Ti/TiO_2 and $Ti/TiO_2/Ta$ NTAs electrodes, respectively.

A distinct layer of nanotubes, approximately 1.55 μm thick, is clearly visible above the Ti substrate and is covered by a protective Pt overlayer, as a result of preparation of the sample for analysis. Based on the contrast in images, the average diameter of the nanotubes, Figures 3 (a) and (d), was determined to be in agreement with values obtained from FE-SEM micrographs. The

View Article Online
DOI: 10.1039/D5CP01788B

calculated lattice spacing in HR-TEM images, Figures 3 (b) and (e), correspond to the (101) and (004) crystal lattice planes of anatase TiO_2, observed for both Ti/TiO_2 and Ti/TiO_2/Ta NTAs (PDF #00-086-1156). The crystalline structure of the nanotubes was analyzed using SAED imaging, with a representative SAED pattern shown in Figure 3 (c) for Ti/TiO_2 NTAs and in Figure 3 (f) for Ti/TiO_2/Ta NTAs. Both patterns feature well-defined concentric rings, characteristic of a fine-grained nanocrystalline structure. The *d*-spacings were estimated based on the radii of the rings, and were summarized in Table 2.

Table 2. Interplanar distances of Ti/TiO_2 and Ti/TiO_2/Ta, determined from the respective SAED diffraction patterns.

***d*-spacings estimated from SAED patterns / nm**		**Miller indices (hkl) (PDF #00-0-86-1156)**
Ti/TiO_2	**Ti/TiO_2/Ta**	
0.352	0.352	Anatase TiO_2 (101)
0.237	0.237	Anatase TiO_2 (004)
-	0.207	β-Ti_2O_5 (330)
0.192	0.190	Anatase TiO_2 (200)
-	0.195	β-Ti_2O_5 (092)
0.171	0.167	Anatase TiO_2 (211)
0.151	0.148	Anatase TiO_2 (204)
0.138	0.136	Anatase TiO_2 (116)
0.129	0.126	Anatase TiO_2 (215)

The corresponding SAED patterns of the samples display reflections characteristic of the anatase TiO_2 phase, and are in good agreement with the XRD analysis. However, in addition to

View Article Online
DOI: 10.1039/D5CP01788B

these anatase reflections, extra diffraction spots are observed for the Ti/TiO_2/Ta sample. The measured *d*-spacings of 0.207 nm and 0.175 nm correspond well with the interplanar distances of the (330) and (092) lattice planes of the orthorhombic β-Ta_2O_5 phase (PDF #00-025-0922). The most common phases of Ta_2O_5 found in thin films include hexagonal δ-Ta_2O_5, orthorhombic β-Ta_2O_5, and tetragonal α-Ta_2O_5, with β-Ta_2O_5 being the most likely phase to occur at low temperatures[34,35]. The presence of Ta_2O_5 was not observed in XRD measurements, most likely due to the low amounts which are below the detection limit of the X-ray diffraction method.

In addition to conventional TEM analysis, the elemental composition of the Ti/TiO_2/Ta NTAs electrode was examined using scanning mode (STEM). Figures 4 (a-c) presents the STEM/HAADF micrograph and the corresponding EDS elemental image maps for titanium, oxygen and tantalum.

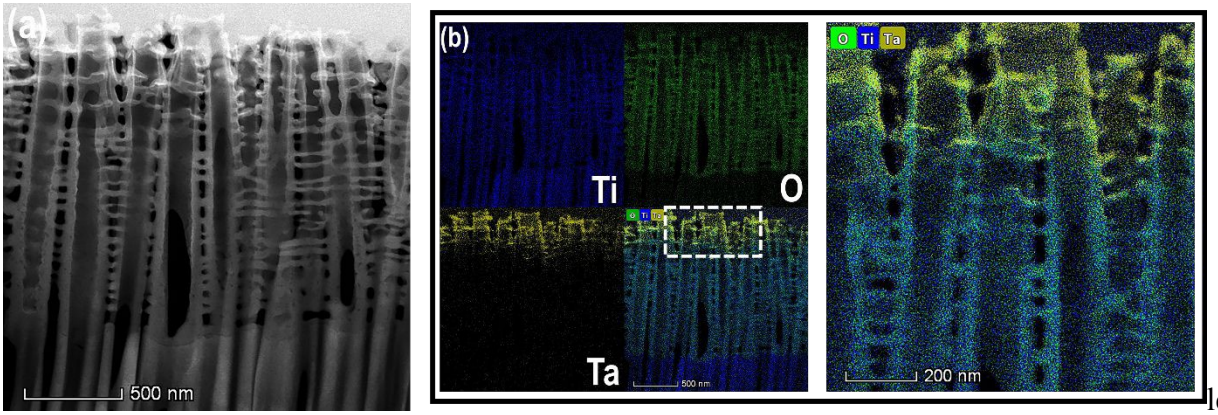

le

Figure 4. STEM/HAADF image of Ti/TiO_2/Ta sample (a) with corresponding EDS maps highlighting the Ti (blue color), O (green color) and Ta (yellow color) elements (b).

In HAADF images, brightness is roughly proportional to the square of the atomic number (Z^2), and the variation in contrast suggests that the topmost part of the nanotubes is covered with

View Article Online
DOI: 10.1039/D5CP01788B

tantalum. However, the contrast difference is somewhat reduced by the protective Pt overlayer. Clearer elemental distributions can be observed in the elemental image maps shown in Figure 4 (b). These images reveal that the Ta layer has penetrated the entire length of the nanotubes, with the highest concentration occurring within the first ~400 nm. Furthermore, quantitative analysis confirmed approximately 33.9 at% of Ta, as shown in Figure S1.

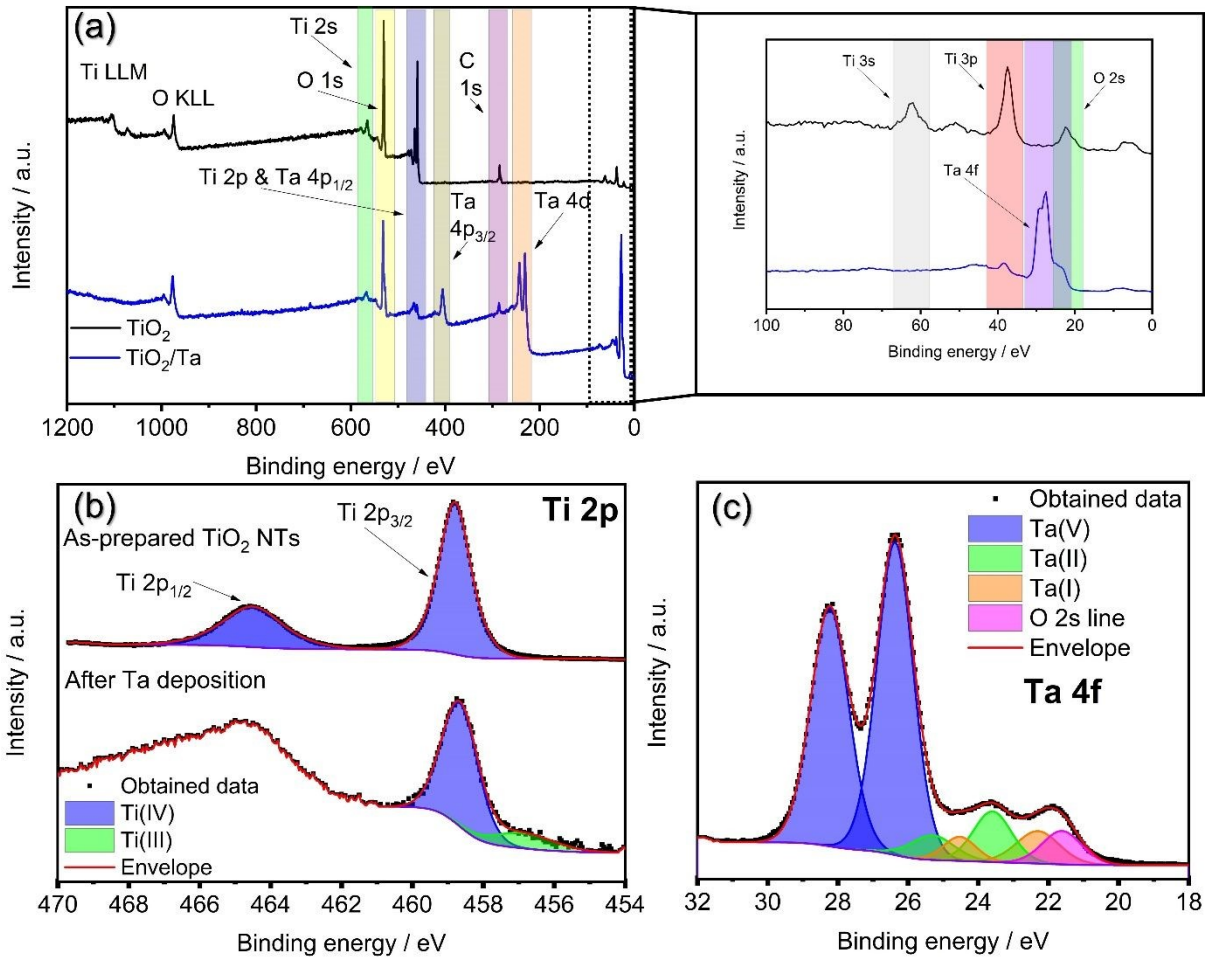

Figure 5. Survey spectra of Ti/TiO_2 and $Ti/TiO_2/Ta$ NTAs electrodes (a); high-resolution XPS analysis: Ti $2p_{3/2}$ and Ti $2p_{1/2}$ lines (b); and Ta $4f_{7/2}$ and Ta $4f_{5/2}$ lines (c).

View Article Online
DOI: 10.1039/D5CP01788B

Chemical bonding – In order to obtain detailed information about the chemical states and bonds between Ti, O, and Ta in the prepared samples, XPS analysis was conducted. The survey spectra for both Ti/TiO_2 and Ti/TiO_2/Ta NTAs are shown in Figure 5 (a). To gain a deeper understanding of the chemical states in our samples, high-resolution XPS spectra of Ti 2p and Ta 4f lines were also obtained, as presented in Figure 5 (b-c).

Both survey spectra reflect the presence of the main photoelectron lines of sample components, including Ti 3p, Ti 3s, Ti 2p and 2s lines, as well as O 1s and 2s lines, and the C 1s line, which indicates organic contamination. The Ti/TiO_2/Ta spectrum reveals additional lines corresponding to Ta 4f, 4d and 4p. Notably, there is a clear decrease in intensity for all Ti-related lines, which directly results from the tantalum sputtering.

Highly symmetric high-resolution XPS spectrum of Ti 2p photoelectron line for the as-prepared TiO_2 NTs, Figure 5 (b) (top), suggests a single contribution. Thus, the Ti 2p doublet, consisting of Ti $2p_{3/2}$ at 458.8 eV and Ti $2p_{1/2}$ at 464.6 eV, was fitted with a single contribution, i.e. Ti(IV). The fitted energies, and the spin-orbit separation of 5.8 eV between the two components are in good agreement with the reported values[36]. In the case of TiO_2 NTs following Ta metal deposition, the spectra in Figure 5 (b) (bottom) shows signs of Ti (IV) reduction, evidenced by the emergence of a new peak at lower binding energy. Due to the significant overlap between the Ti $2p_{1/2}$ core-level and the Ta $4p_{1/2}$ energy range, the Ti $2p_{1/2}$ region was not deconvoluted. As a result, the analysis of titanium chemical states was based solely on the Ti $2p_{3/2}$ peak, which remains unaffected by this overlap and allows for a more accurate assessment of Ti oxidation states. By means of active fitting analysis, it was determined that ~17 at.% of Ti (IV) was reduced to Ti (III).

View Article Online
DOI: 10.1039/D5CP01788B

In previous studies, C.-H. Hsu et al[37] have suggested that Ta dopants create oxygen vacancies and reduce Ti (IV) to Ti (III), with higher levels of tantalum incorporation leading to further reduction to Ti (II). Similarly, L. M. Vincente-Arche et al[38] reached comparable conclusions.

High-resolution spectrum of Ta 4f photoelectron line, Figure 5 (c), was fitted with 3 Ta-related contributions (doublets). In addition, one O 2s singlet contribution was added as it falls under this binding energy region also observed in survey spectrum, Figure 5 (a). Each doublet is composed of Ta $4f_{7/2}$ and $4f_{5/2}$ lines. Binding energies of each component were determined from the best fit results, and are summarized in Table 3.

Table 3. Ta 4f binding energies obtained from the peak fits, Figure 5 (c).

Oxidation states	**Binding energies / eV**	
	Ta $4f_{7/2}$	**Ta $4f_{5/2}$**
Ta(I)	22.3	24.4
Ta(II)	23.5	25.3
Ta(V)	26.3	28.2

In addition to Ta_2O_5, which was observed in the TEM analysis, two sub-oxide reduction states were identified – TaO and Ta_2O. The peak positions and spin-orbit separation of ~1.9 eV are in agreement with previously reported values.[39,40] It can be concluded that the oxidation of Ta to Ta_2O_5 along with the presence of lower concentrations of TaO and Ta_2O, indicates that a redox reaction occurs when thin films of one metal are deposited on an oxide surface.[41,42] This conclusion is further supported by the observation of the partial reduction of the metal oxide on which the metal was deposited. Specifically, the partial reduction of Ti^{4+} to Ti^{3+} was noted. This implies that,

View Article Online
DOI: 10.1039/D5CP01788B

along with oxidation from air, oxygen from TiO_2 diffused to the surface to oxidize the Ta film, leaving no trace of metallic Ta.

Electrical properties – Specific electrical conductivity of Ti/TiO_2 and $Ti/TiO_2/Ta$ electrodes was evaluated by four-point probe method, at room temperature. Due to the porous morphology of the samples, measurements were taken from several different surface areas, and by changing the applied current by an order of magnitude. Obtained values are presented in Table 4.

Table 4. Specific electrical conductivity of Ti/TiO_2 and $Ti/TiO_2/Ta$ NTAs at various current values, at room temperature.

I / μA	**σ / S·cm^{-1}**	
	Ti/TiO_2	**$Ti/TiO_2/Ta$**
0.01	$(1.33 – 1.58)\cdot10^{-5}$	$(1.95 – 2.07)\cdot10^{-4}$
0.1	$(2.87 – 4.02)\cdot10^{-4}$	$(3.12 – 4.08)\cdot10^{-3}$
1	$(4.24 – 5.51)\cdot10^{-3}$	$(2.94 – 3.57)\cdot10^{-2}$
10	$(2.02 – 2.37)\cdot10^{-2}$	$(2.70 – 3.22)\cdot10^{-1}$

For all applied current rates, the specific electrical conductivity of Ti/TiO_2 is approximately one order of magnitude lower than that of $Ti/TiO_2/Ta$.

Optical properties **–** To explore the impact of Ta-metal sputtering on the optical band gap, E_g, DR UV-Vis spectra were recorded of both for Ti/TiO_2 NTAs and $Ti/TiO_2/Ta$ NTAs electrodes. For presenting obtained spectra, Kubelka-Munk (KM) function, which is ratio of absorption coefficient k and scattering coefficient s (i.e. k/s), was calculated from relative reflectance R'_∞ according to equation (1):

View Article Online
DOI: 10.1039/D5CP01788B

$$F(R'_\infty) = \frac{(1-R'_\infty)^2}{2R'_\infty} \quad (1)$$

In Figure 6 (a) the significant increase of light absorption in visible region of spectra can be observed after Ta sputtering i.e. for Ti/TiO_2/Ta NTAs electrode. A Tauc plot, $(F(R'_\infty)\cdot h\upsilon)^{1/n}$ vs. hν, was used to estimate the band gap, where $n = 1/2$ is taken for materials with a direct band gap and $n = 2$ for those with an indirect band gap. Anatase TiO_2 is a known semiconducting material with indirect band gap. For the sample modified with Ta, TEM analysis confirmed the presence of orthorhombic β-Ta_2O_5 phase on the surface of the TiO_2 nanotubes. Direct band gap transitions are characteristic of β-Ta_2O_5. The E_g of TiO_2 NTs is determined by extrapolating the linear portion of the plot to the x-axis, and is found to be 3.05 eV (Figure 6 (b)).[43]

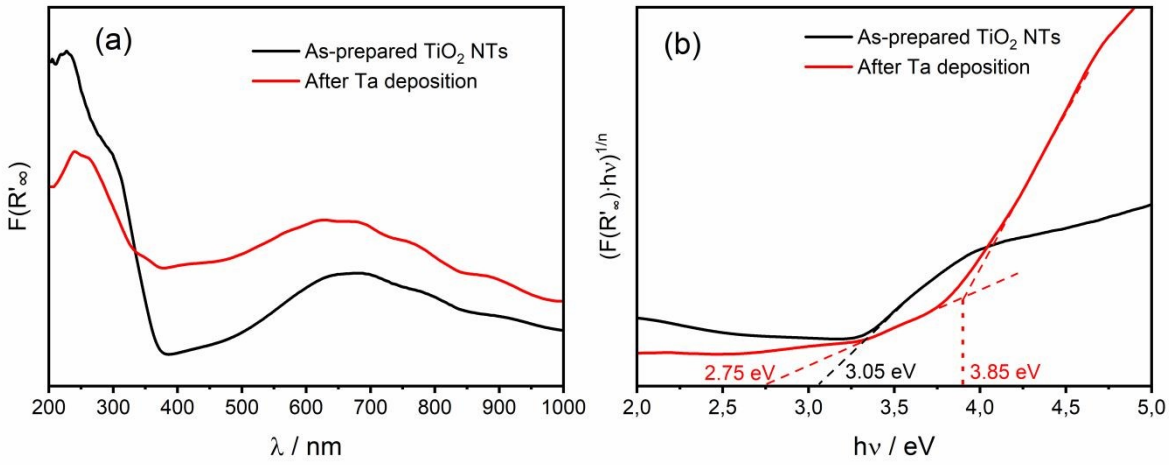

Figure 6. Kubelka-Munk function of as-prepared TiO_2 NTs, and after Ta deposition (a) and corresponding Tauc plots (b).

The Tauc plot derived from UV-Vis spectra of the Ti/TiO_2/Ta NTs exhibit two linear regions, a characteristic often observed in composite structures or surface-modified materials. Both linear portions should be considered, as illustrated in Figure 6 (b). The determined band gap of

View Article Online
DOI: 10.1039/D5CP01788B

3.85 eV is consistent with reported values for β-Ta_2O_5[44]. It is also worth noting that following modification with sputtered Ta, the electrode color changed from blue (after electrochemical anodization and annealing) to black (Figure S2). This color change, supported by optical characterization, is potentially attributable to the parallel formation of a black Ta_2O_5 phase[45], which may also explain the observed additional absorption edge at 2.75 eV for the Ta-deposited sample.

Despite exhibiting a larger band gap, electrical measurements revealed higher conductivity in the Ta-deposited samples compared to TiO_2 nanotubes. This increased conductivity is likely associated with the Ta-induced reduction of Ti^{4+} to Ti^{3+}, a finding corroborated by XPS analysis, and could be further enhanced by the presence of the black Ta_2O_5 phase.

Photoluminescence (PL) spectroscopy provides valuable insights into the electronic structure of materials, particularly regarding the presence of localized electronic states within the bandgap of the oxide layer. In metal-oxide-based semiconductors, the concentration of point defects and oxygen activity in the lattice play an important role in determining their electrical properties. A comparative analysis of the PL spectra of TiO_2 NTs and Ta-modified TiO_2 NTs enables the identification of interaction processes between TiO_2 and the Ta_2O_5 layer on its surface.

A detailed explanation of the possible formed point defects and the origin of radiative recombination processes observed in the PL emission spectra of anatase TiO_2 NTs is provided in our previous work[46]. The focus of discussion was the roles of defect states and their influence on the electrical and optical properties of the material. The PL spectra of TiO_2 NTs and Ta-modified TiO_2 NTs are presented on Figure 7, with excitation energy at 380 nm. The obtained PL spectra of

View Article Online
DOI: 10.1039/D5CP01788B

TiO_2 NTs exhibit a broad emission peak spanning from 400 to 600 nm, which can be deconvoluted into five Gaussian contribution peaks with maxima at 403, 435, 465, 497, and 545 nm. These peak maxima correspond to intraband states with associated energies of 3.08, 2.85, 2.67, 2.50, and 2.27 eV, respectively. In contrast, the PL spectra of Ta-modified TiO_2 NTs show a reduction in overall PL intensity. Between 400 and 500 nm, the PL intensity is partially suppressed, while from 500 to 600 nm, almost no light emission is observed. This spectrum can be deconvoluted into three Gaussian contribution peaks with maxima at 403, 437, and 470 nm, corresponding to intraband states with energies of 3.08, 2.84, and 2.60 eV, respectively. In anatase TiO_2, high-energy peaks are attributed to transitions between the valence band and the conduction band edges. We observe, for both materials, indirect band transitions $X_{2b}\rightarrow\Gamma_{1b}$ and $X_{1a}\rightarrow\Gamma_{1b}$ with energy of 3.08 eV and 2.85 eV, respectively. Literature suggests that peaks at energies below conduction band are induced by the presence of oxygen vacancies surface states (V_o).[47] Surface states are sharp energy levels with a much lower density of states compared to the broad conduction and valence bands. These states can significantly alter the electrical properties of materials and can be introduced in a controlled manner through doping or surface modification.[48] For Ta-modified TiO_2 NTs PL spectra had an altered shape, where recombination from $X_{2b}\rightarrow\Gamma_{1b}$ mostly contributes to PL intensity. It can be concluded that modification of TiO_2 with Ta eliminated recombination from deep defect states within the bandgap. Because XPS analysis revealed an increase in oxygen vacancies in the modified TiO_2, the lower PL intensity can be attributed to the fact that the unpaired electrons in vacancy induced surface states exhibit a lower recombination rate. This contributes to an overall increase in charge carrier density and enhanced conductivity.

View Article Online
DOI: 10.1039/D5CP01788B

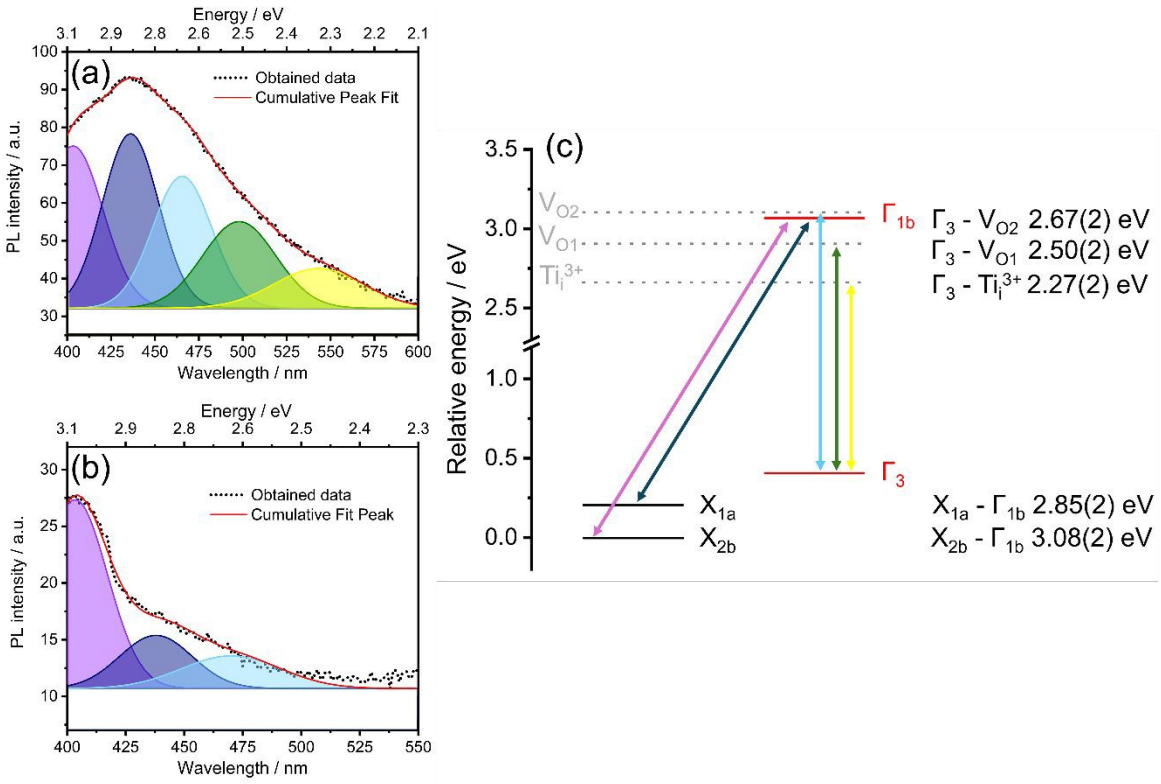

Figure 7. PL emission spectra (λ_{ex}=370 nm) of as-prepared TiO_2 NTs (a), after Ta deposition (b), along with a simplified energy diagram (c), constructed from PL data.

Electrochemical experiments – To evaluate the electrochemical performance of Ti/TiO_2 NTAs and Ti/TiO_2/Ta NTAs electrodes as potential anode materials for Li-ion batteries, GS cycling and EIS experiments were performed. To obtain better comparation of the electrochemical properties of these two electrodes, the measurements were performed at different temperatures.

GS experiments were performed divided in two sets: one at a constant temperature of 25°C with varying current rates, and the other with constant current rates across the temperature range from 25 to 55°C, as shown in Figure 8 (a-d). Current rates were calculated by taking 1C = 167.5 $mAh \cdot g^{-1}$.

View Article Online
DOI: 10.1039/D5CP01788B

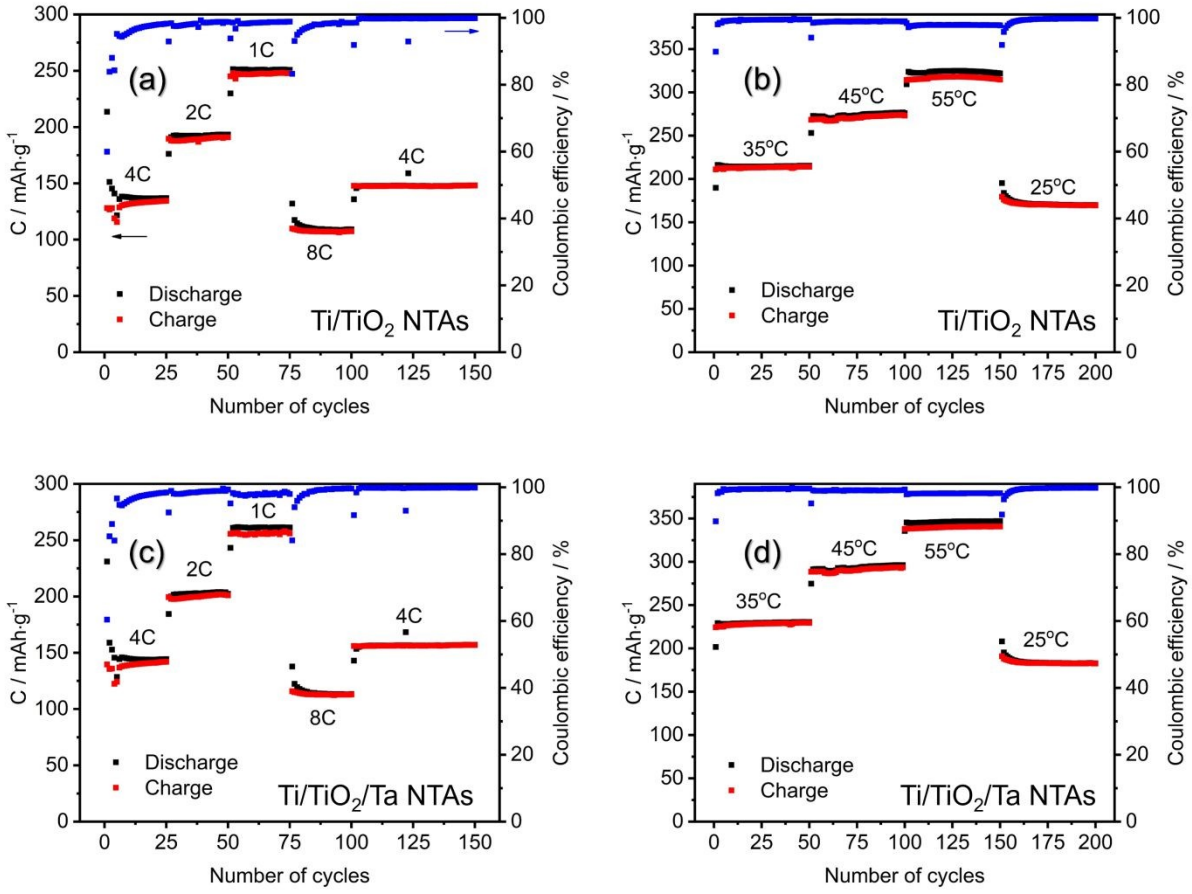

Figure 8. Discharge/charge performance of: (a) Ti/TiO_2 NTAs and (c) Ti/TiO_2/Ta NTAs electrodes at different current rates and at different temperatures at current rate 4C, (b) and (d), respectively.

Both electrodes show an initial capacity fade due to irreversible loss, but after 25 cycles at 4C, the (de)intercalation process stabilizes. At 25°C, at all current rates, Ti/TiO_2/Ta NTAs electrode shows somewhat higher capacity values and Coulombic efficiency equal or slightly higher comparing to Ti/TiO_2 NTAs electrode. Discharge capacities and Coulombic efficiencies (CE) for both electrodes are summarized in Table 5.

View Article Online
DOI: 10.1039/D5CP01788B

Table 5. Summary of discharge capacities and Coulombic efficiencies for Ti/TiO_2 NTAs and $Ti/TiO_2/Ta$ NTAs electrodes.

Current Rate / C	Number of cycles	Temperature / °C	Discharge capacity Ti/TiO_2 NTAs / $mAh \cdot g^{-1}$	Ti/TiO_2 NTs CE / %	Discharge capacity $Ti/TiO_2/Ta$ NTAs /$mAh \cdot g^{-1}$	$Ti/TiO_2/Ta$ CE / %
4	25	25	136.8	98.3	144.3	98.5
2	25	25	193.3	98.8	203.5	98.8
1	25	25	250.8	99.7	261.3	99.7
8	25	25	109.0	98.5	113.4	99.6
4	50	25	148.2	98.3	157.1	98.5
4	50	35	215.2	99.6	230.5	99.6
4	50	45	276.0	98.9	296.1	99.2
4	50	55	322.0	97.8	347.1	98.2

At higher temperatures (35, 45, and 55°C) at current rate 4C, the capacity values of $Ti/TiO_2/Ta$ NTAs electrode slightly increase during 50 cycles, which is not the case with Ti/TiO_2 NTAs electrode at 35°C and 55°C, Figures 8 (b) and (d). The discharge capacity difference between two electrodes increases with increasing temperature in the favor of $Ti/TiO_2/Ta$ NTAs electrode, Table 5. This increase amounts to 7.1, 7,3 and 7.8% at 35, 45 and 55°C, while at 25°C it is 6.0%. The Coulombic efficiency decreases with increasing temperature as a consequence of increased electrolyte decomposition but generally is slightly higher after Ta sputtering. Better performance of $Ti/TiO_2/Ta$ NTAs electrode was obtained despite the fact that Ta sputtering reduces the inner diameter and the space between NTs, which can affect their wetting with

View Article Online
DOI: 10.1039/D5CP01788B

electrolyte from inside and outside. The voltage profiles at different current rates and different temperatures, being very similar for both electrodes, are shown in S4.

Table 6 presents a comparative overview of recent literature about the specific capacities of various TiO_2-based anode materials, evaluated at high current rates and prepared using different synthetic approaches. In our case, subsequent modification with a Ta layer via DC sputtering slightly increases the capacity from 250.8 to 261.3 $mAh \cdot g^{-1}$ under the same current density. These values are notably higher than other reported values.[49,50,51,53,54]

TiO_2 thin wall NTs obtained by anodization demonstrate the highest capacity among recent literature (302.7 $mAh \cdot g^{-1}$ at 1.325C).[52] Recently, mechanochemically prepared TiO_2 nanostructures from $Li_4Ti_5O_{12}$ present a moderate capacity of 122 $mAh \cdot g^{-1}$ at 1.5C,[53] while TiO_x nanosheets reduced in a H_2/Ar atmosphere reach 147.6 $mAh \cdot g^{-1}$ at 1C.[54]

Table 6. Electrochemical performance of various TiO_2-based anode materials

Material	**Preparation Method**	**Current rate**	**Specific capacity**	**Reference**
TiO_2 NTs	anodization	1C	250.8 mAh□g^{-1}	This work
TiO_2/Ta NTs	anodization + DC sputtering	1C	261.3 mAh□g^{-1}	This work
TiO_2/graphene nanosheets	Solvothermal	1C	161 mAh□g^{-1}	49
TiO_2 hierarchical nanosheets	Solvothermal	1C	225 mAh□g^{-1}	50

View Article Online
DOI: 10.1039/D5CP01788B

TiO_2@C hollow spheres	Hydrothermal	2C	70 mAh□g^{-1}	51
TiO_2 thin wall NTs	Anodization	1.325 C	302.7 mAh·g^{-1}	52
TiO_2 nanostructures	High–energy mechanical milling of $Li_4Ti_5O_{12}$	1.5 C	122 mAh·g^{-1}	53
TiO_x nanosheets	Reduced in H_2/Ar atmosphere	1C	147.6 mAh·g^{-1}	54

EIS measurements were performed at 25-55 °C using the same cells as for GS cycling. Before the measurements, the electrodes were galvanostatically lithiated, then halfway delithiated and allowed to relax until constant potential was reached, at each temperature. Obtained Nyquist plots are shown in Figure 9 (a-d). The same equivalent circuit (EC), presented in the insets of the graphs, was used for fitting EIS data at all temperatures. Deviation on lower frequencies from plotted graph that can be seen on Figure 9 (d) is attributed to charge accumulation at the electrode interface, characteristic of capacitive processes.[55] Such behavior is not manifested at lower temperatures.

View Article Online
DOI: 10.1039/D5CP01788B

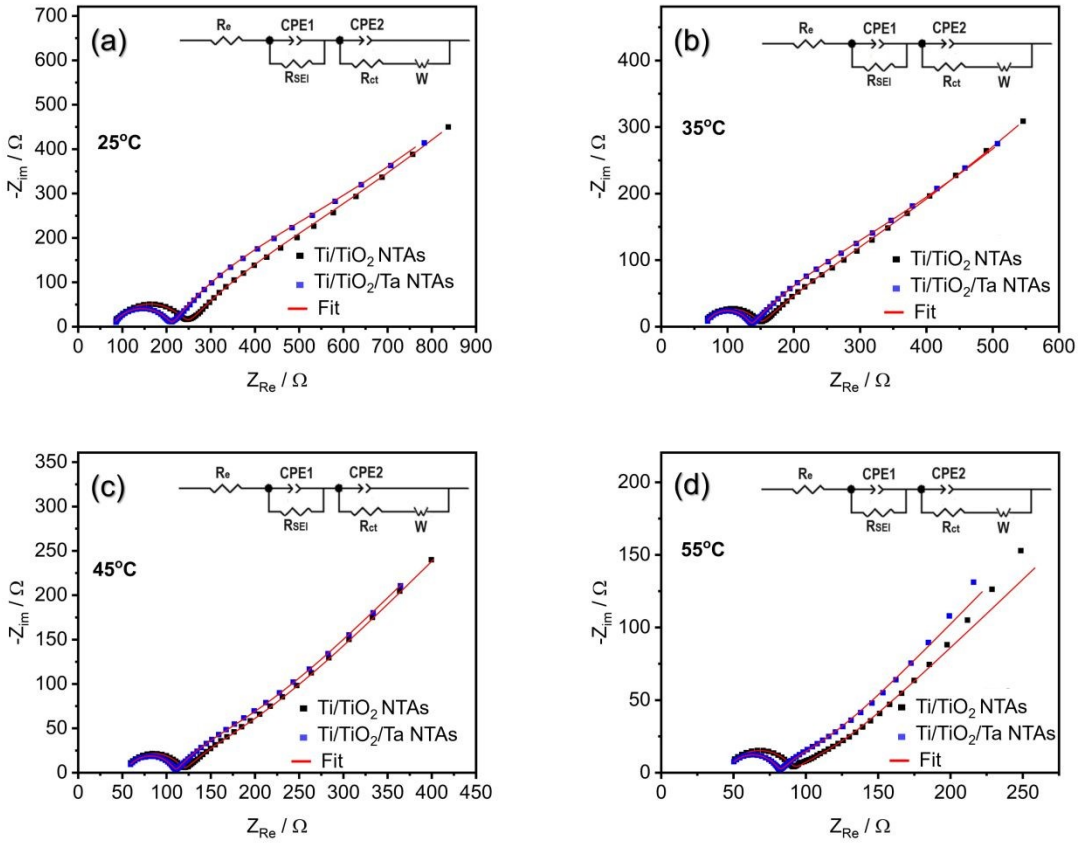

Figure 9. Nyquist plots obtained by EIS for Ti/TiO_2 and $Ti/TiO_2/Ta$ at 25°C (a); 35°C (b); 45°C (c) and 55°C (d).

In the equivalent circuit, R_e is the electrolyte resistance, R_{SEI} is the solid electrolyte interface resistance (surface film resistance), while charge transfer resistance is designated as R_{ct}. CPE is constant phase element, and W presents Warburg diffusion impedance. All resistances obtained as a result of data fitting, except R_e which does not depend on the electrode type, are shown in Table 7. Li-ion diffusion coefficients, obtained from EIS data fitting, are also presented

View Article Online
DOI: 10.1039/D5CP01788B

in Table 7. A detailed explanation of how the calculation was carried out is given in the Supplementary Material.

Table 7. Resistances and Li-ion diffusion coefficients derived from the fitting of EIS data.

T / °C	Ti/TiO_2 NTAs			$Ti/TiO_2/Ta$ NTAs		
	R_{SEI} / Ω	R_{ct} / Ω	D / $cm^2 \cdot s^{-1}$	R_{SEI} / Ω	R_{ct} / Ω	D / $cm^2 \cdot s^{-1}$
25	170	906	$1.6 \cdot 10^{-18}$	136	672	$1.9 \cdot 10^{-18}$
35	88	658	$3.7 \cdot 10^{-18}$	70	528	$5.6 \cdot 10^{-18}$
45	67	186	$9.2 \cdot 10^{-18}$	56	161	$1.8 \cdot 10^{-17}$
55	47	68	$3.2 \cdot 10^{-17}$	37	55	$6.9 \cdot 10^{-17}$

It can be seen from Table 7, that R_{SEI} and R_{ct} decrease and diffusion coefficient (D) increases, with increasing temperature. This is in agreement with obtained increase in capacity values of Ti/TiO_2 and $Ti/TiO_2/Ta$ NTAs electrodes with temperature rise (Figure 8 (b) and 8 (d)). The lower R_{SEI} values observed in the case of the $Ti/TiO_2/Ta$ NTAs electrode indicate a change in the composition or thickness of the film on this electrode, compared to Ti/TiO_2 NTAs electrode. The lower values of R_{ct} for $Ti/TiO_2/Ta$ NTAs electrodes can be correlated to higher electrical conductivity, compared to Ti/TiO_2 electrode. The increase in charge carrier density comes from larger number of oxygen vacancies in Ta-modified electrode, as mentioned before in PL and XPS analyses.

The overlapping of the second semicircle with the linear part is present at all temperatures and indicates mixed kinetic and diffusion control of Li-ion insertion/deinsertion process. The

View Article Online
DOI: 10.1039/D5CP01788B

decrease in both R_{SEI} R_{ct} with expected increase in diffusion coefficient D, with increasing temperature are the cause of the slight increase in Li^+-ion intercalation/deintercalation capacity of TiO_2 NTs after Ta deposition (Table 7). Herein obtained Li-ion diffusion coefficients are in good agreement (same order of magnitude) with our previously reported values for thin-wall TiO_2 NTs.[52]

4. Conclusion

Our approach to modifying the optical and electrical properties of TiO_2 NTs involved depositing tantalum via sputtering. This process induces oxygen diffusion from the TiO_2 lattice, resulting in the formation of crystalline β-Ta_2O_5, as confirmed by selected area electron diffraction. Resistivity measurements of the NTs have shown an increase in conductivity, approximately one order of magnitude. Additionally, EIS measurements suggest a reduction in charge transfer resistance, which could be attributed to the higher number of free electrons in the modified material. Despite the improved electrical conductivity, an increase in the optical effective bandgap from 3.05 to 3.85 eV was noted. We attribute the enhancement in conductivity to the Ta-induced reduction of Ti^{4+} to Ti^{3+}, a finding confirmed by XPS analysis, and presence of black Ta_2O_5 with additional bandgap transition at lower energies of 2.75 eV. The sputtering process also led to the suppression of deep-level trap states within the bandgap, which were observed in as-prepared TiO_2 NTs. Given that β-Ta_2O_5 is known for its stability at high temperatures, the modified material was tested as a potential anode for Li-ion batteries at elevated temperatures. Compared to as-prepared TiO_2 NTs, the modified material exhibited a slight increase in capacity and higher Coulombic efficiencies, particularly at elevated temperatures.

View Article Online
DOI: 10.1039/D5CP01788B

Conflict of interest

There are no conflicts to declare.

Data availability

The data corresponding to Electrochemical tests is available in Supplementary material. Other data that support the findings of this study are available from the corresponding author upon reasonable request.

Acknowledgments

This work was financially supported by the Ministry of Science, Tehnological Development and Innovation of the Republic of Serbian, contract number(s): 451-03-136/2025-03/200017 and 451-03-136/2025-03/200175. Authors would like to thank Dr. Vladimir Rajic and Dr. Milutin Ivanovic for their help with SEM and XPS acquisitions, and Dr. Mirjana Novaković for proofreading the text.

View Article Online
DOI: 10.1039/D5CP01788B

References

1. Gerischer H. The impact of semiconductors on the concepts of electrochemistry. *Electrochim Acta*. 1990;35:1677. Doi: https://doi.org/10.1016/0013-4686(90)87067-C

2. Singh K, Nowotny J, Thangadurai V. Amphoteric oxide semiconductors for energy conversion devices: A tutorial review. *Chem Soc Rev*. 2013;42:1961–72. Doi: https://doi.org/10.1039/c2cs35393h

3. Zhu B, Fan L, Mushtaq N, Raza R, Sajid M, Wu Y, Lin W, Kim JS, Lund PD, Yun S. Semiconductor electrochemistry for clean energy conversion and storage. Electrochem Energy Rev. 2021;4:757-792. Doi: https://doi.org/10.1007/s41918-021-00112-8

4. Balaya P. Size effects and nanostructured materials for energy applications. *Energy Environ Sci*. 2008;1:645–54. Doi: https://doi:10.1039/b812394n

5. Piyadasa A, Wang S, Gao PX. Band structure engineering strategies of metal oxide semiconductor nanowires and related nanostructures: A review. *Semicond Sci Technol*. 2017;32(7):073001. Doi: https://doi.org/10.1088/1361-6641/aa6778

6. Hu X, Li G, Yu JC. Design, fabrication, and modification of nanostructured semiconductor materials for environmental and energy applications. *Langmuir*. 2010;26(7):3031–9. Doi: https://doi.org/10.1021/la902142b

7. Lee K, Mazare A, Schmuki P. One-dimensional titanium dioxide nanomaterials: Nanotubes. *Chem Rev*. 2014;114(19):9385–454. Doi: https://doi.org/10.1021/cr500061m

View Article Online
DOI: 10.1039/D5CP01788B

8. Munonde TS, Raphulu MC. Review on titanium dioxide nanostructured electrode materials for high-performance lithium batteries. *J Energy Storage*. 2024;78:110064. Doi: https://doi.org/10.1016/j.est.2023.110064

9. Kapilashrami M, Zhang Y, Liu YS, Hagfeldt A, Guo J. Probing the optical property and electronic structure of TiO_2 nanomaterials for renewable energy applications. *Chem Rev*. 2014;114(19):9662–707. Doi: https://doi.org/10.1021/cr5000893

10. Choi WH, Lee CH, Kim H, Lee SU, Bang JH. Designing a high-performance nitrogen-doped titanium dioxide anode material for lithium-ion batteries by unraveling the nitrogen doping effect. *Nano Energy*. 2020;74:104829. Doi: https://doi.org/10.1016/j.nanoen.2020.104829

11. He Q, Sun Z, Shi X, Wu W, Cheng J, Zhuo R, Zhang Z, Wang J. Electrochemical performance enhancement of nitrogen-doped TiO2 for lithium-ion batteries investigated by a film electrode model. *Energy Fuels*. 2021;35:2717. Doi: https://doi.org/10.1021/acs.energyfuels.0c03580

12. Li H, Li Y, Zhao X, Wang Y, Huang K, Qiu W, Wang J, Liu J. Vacancy-induced anion and cation redox chemistry in cation-deficient F-doped anatase TiO2. *J Mater Chem A*. 2020;8:20393-20401. Doi: https://doi.org/10.1039/d0ta07578g

13. Jeong JH, Jung DW, Shin EW, Oh ES. Boron-doped TiO_2 anode materials for high-rate lithium-ion batteries. *J Alloys Compd*. 2014;604:226–32. Doi: https://doi.org/10.1016/j.jallcom.2014.03.069

View Article Online
DOI: 10.1039/D5CP01788B

14. Ko WY, Wu TC, He SY, Lin KJ. Phosphorus-doped TiO_2 mesoporous nanocrystals for anodes in high-current-rate lithium-ion batteries. *Nanotechnology*. 2024;35:175403. Doi: https://doi.org/10.1088/1361-6528/ad22aa

15. Fan Y, Chen X, Zhang K, Rong J, Yu X. A coordinated regulation strategy to improve electronic conductivity and Li-ion transport for TiO_2 lithium battery anode materials. *J Alloys Compd*. 2021;860:158282. Doi: https://doi.org/10.1016/j.jallcom.2020.158282

16. Bhasin V, Halankar KK, Biswas A, Ghosh SK, Sarkar SK, Jha SN, Bhattacharyya D. Improvement of high current performance of Li-ion batteries with TiO_2 thin film anodes by transition metal doping. *J Alloys Compd*. 2023;942:169118. Doi: https://doi.org/10.1016/j.jallcom.2023.169118

17. Usui H, Domi Y, Yamamoto Y, Hoshi T, Tanaka T, Oishi N, Nitta N, Sakaguchi H. Nickel-doped titanium oxide with layered rock-salt structure for advanced Li-storage materials. *ACS Appl Energy Mater*. 2023;5:6292-304. Doi: https://doi.org/10.1021/acsaelm.3c01162

18. Usui H, Domi Y, Takama K, Tanaka Y, Sakaguchi H. Tantalum-doped titanium dioxide with rutile structure as a novel anode material for sodium-ion battery. *ACS Appl Energy Mater*. 2019;2:3056–60. Doi: https://doi.org/10.1021/acsaem.9b00585

19. Ahmed ATA, Soni R, Ansari AS, Lee CY, Kim HS, Im H, Bathula C. Biowaste-derived graphitic carbon interfaced TiO_2 as anode for lithium-ion battery. *Surf Interfaces*. 2022;35:102404. Doi: https://doi.org/10.1016/j.surfin.2022.102404

View Article Online
DOI: 10.1039/D5CP01788B

20. Lu X, Luo F, Tian Q, Zhang W, Sui Z, Chen J. Anatase TiO_2 nanowires intertangled with CNT for conductive additive-free lithium-ion battery anodes. *J Phys Chem Solids*. 2021;153:110037. Doi: https://doi.org/10.1016/j.jpcs.2021.110037

21. Sidoli M, Magnani G, Fornasini L, Scaravonati S, Morenghi A, Vezzoni V, Bersani D, Bertoni G, Gaboardi M, Ricco M, Pontiroli D. Defective graphene decorated with TiO_2 nanoparticles as negative electrode in Li-ion batteries. J Alloys Compd. 2023;958:170420. Doi: https://doi.org/10.1016/j.jallcom.2023.170420

22. Lu Q, Meng X, Omar A, Mikhailova D, Cao R, Jiao S, Lu Y, Xu Y. Carbon materials for stable Li metal anodes: Challenges, solutions, and outlook. *Carbon Energy*. 2021;3:957–975. Doi: https://doi.org/10.1002/cey2.147

23. Savva AI, Smith KA, Lawson M, Croft SR, Weltner AE, Jones CD, Bull H, Simmons PJ, Li L, Xiong H. Defect generation in TiO_2 nanotube anodes via heat treatment in various atmospheres for lithium-ion batteries. *Phys Chem Chem Phys*. 2018;20:22537–22546. Doi: https://doi.org/10.1039/C8CP04368J

24. Qiao Z, Lin L, Yan X, Guo W, Chen Q, Xie Q, Han X, Lin J, Wang L, Peng DL. Function and application of defect chemistry in high-capacity electrode materials for Li-based batteries. *Chem Asian J*. 2020;15:3620–3636. Doi: https://doi.org/10.1002/asia.202000904

25. Reynaud M, Serrano-Sevillano J, Casas-Cabanas M. Imperfect battery materials: A closer look at the role of defect. *Chem Mater*. 2023;35(9):3345–3363. Doi: https://doi.org/10.1021/acs.chemmater.2c03481

View Article Online
DOI: 10.1039/D5CP01788B

26. Zhang Y, Tao L, Xie C, Wang D, Zou Y, Chen R, Wang Y, Jia C, Wang S. Defect engineering on electrode materials for rechargeable batteries. *Adv Mater*. 2020;32:1905923. Doi: https://doi.org/10.1002/adma.201905923

27. Fu H, Wen Q, Li PY, Wang Z, He Z, Yan C, Mao J, Dai K, Zhang X, Zheng J. Recent advances on heterojunction-type anode materials for lithium-/sodium-ion batteries. *Small Methods*. 2022;6:2201025. Doi: https://doi.org/10.1002/smtd.202201025

28. Kong X, Su Y, Xing C, Cheng W, Huang J, Zhang L, Ouyang H, Feng Q. Facile synthesis of porous TiO_2/SnO_2 nanocomposites as lithium ion battery anode with enhanced cycling stability via nanoconfinement effect. *Chin Chem Lett*. 2023;35:109428. Doi: https://doi.org/10.1016/j.cclet.2023.109428

29. Ma Y, Zhang L, Chai Z, Huang X, Ding B, Ahsan Z, Song G, Xu Y, Yang W, Wen C. Study of TiO_2-coated α-Fe_2O_3 composites and the oxygen-defects effect on the application as the anode materials of high-performance Li-ion batteries. *ACS Appl Energy Mater*. 2020;3:11666–11673. Doi: https://doi.org/10.1021/acsaem.0c01661

30. Gomez K, Fletes E, Parsons JG, Alcoutlabi M. The effect of TiO_2 on the electrochemical properties of Sb_2O_3 anodes for Li-ion batteries. *Appl Sci*. 2024;14:6598. Doi: https://doi.org/10.3390/app14156598

31. Lee G, Kim S, Kim S, Choi J. SiO_2/TiO_2 composite film for high capacity and excellent cycling stability in lithium-ion battery anodes. *Adv Funct Mater*. 2017;27:1703538. Doi: https://doi.org/10.1002/adfm.201703538

View Article Online
DOI: 10.1039/D5CP01788B

32. Cheary RW, Coelho AA. A fundamental parameters approach of X-ray line-profile fitting. J Appl Cryst. 1992;25:109, https://doi.org/10.1107/S0021889891010804

33. A. Le Bail, Whole Powder Pattern Decomposition Methods and Applications: A Retrospection. Powder Diffr. 20 (2005) 316, https://doi.org/10.1154/1.2135315

34. Devan RS, Ho WD, Lin JH, Wu SY, Ma YR, Lee PC. X-ray diffraction study of a large-scale and high-density array of one-dimensional crystalline tantalum pentoxide nanorods. *Cryst Growth Des*. 2008;8:4465–4468. Doi: https://doi.org/10.1021/cg800369s

35. Mohammadi MR, Fray DJ, Sadrnezhaad SK, Mohammadi A. A simple particulate sol-gel route to synthesize nanostructural TiO_2-Ta_2O_5 binary oxides and their characteristics. *Mater Sci Eng B*. 2007;142:16–27. Doi: https://doi.org/10.1016/j.mseb.2007.06.023

36. Biesinger MC, Lau LWM, Gerson AR, Smart RSC. Resolving surface chemical states in XPS analysis of first row transition metals, oxides and hydroxides: Sc, Ti, V, Cu and Zn. *Appl Surf Sci*. 2010;257:887–898. doi: https://doi.org/10.1016/j.apsusc.2010.07.086

37. Hsu CH, Chen KT, Lin LY, Wu WY, Liang LS, Gao P, Qiu Y, Zhang XY, Huang PH, Lien SY, Zhu WZ. Tantalum-doped TiO_2 prepared by atomic layer deposition and its application in perovskite solar cells. *Nanomaterials*. 2021;11:1504. Doi: https://doi.org/10.3390/nano11061504

38. Vincente-Arche LM, Mallik S, Cosset-Cheneau M, Noel P, Vaz DC, Trier F, Gosavi TA, Lin CC, Nikonov DE, Young IA, Sander A, Barthelemy A, Attane JP, Vila L, Bibes M. Metal/$SrTiO_3$ two-dimensional electron gases for spin-to-charge conversion. *Phys Rev Mater*. 2021;5:064005. Doi: https://doi.org/10.1103/PhysRevMaterials.5.064005

View Article Online
DOI: 10.1039/D5CP01788B

39. Simpson R, White RG, Watts JF, Baker MA. XPS investigation of monoatomic and cluster argon ion sputtering of tantalum pentoxide. *Appl Surf Sci*. 2017;405:79–87. Doi: https://doi.org/10.1016/j.apsusc.2017.02.006

40. Benito N, Palacio C. Nanostructuring of Ta_2O_5 surfaces by low energy Ar^+ bombardment. *Appl Surf Sci*. 2015;351:753–759. Doi: https://doi.org/10.1016/j.apsusc.2015.05.143

41. Dahal S, Rana D, Sinkovic B. NiO surface reduction by Nd overlayers. *Vacuum*. 2024;224:113108. Doi: https://doi.org/10.1016/j.vacuum.2024.113108

42. Picone A, Riva M, Brambila A, Calloni A, Bussetti G, Finazzi M, Ciccacci F, Duo L. Reactive metal–oxide interfaces: A microscopic view. *Surface Sci Rep*. 2016;71:32–76. Doi: https://doi.org/10.1016/j.surfrep.2016.01.003

43. Lopez R, Gomez R. Band-gap energy estimation from diffuse reflectance measurement on sol-gel and commercial TiO_2: a comparative study. *J Sol-Gel Sci Technol*. 2012;61:1–7. Doi: https://doi.org/10.1007/s10971-011-2582-9

44. Sathasivam S, Williamson BAD, Kafizis A, Althabaiti SA, Obaid AY, Basahed SN, Scanlon DO, Carmalt CJ, Parkin IP. Computational and experimental study of Ta_2O_5 thin films. *J Phys Chem C*. 2017;121:202–210. Doi: https://doi.org/10.1021/acs.jpcc.6b11073

45. Ding D, Xie Y, Li K, Huang L, Zheng X. Black plasma-sprayed Ta_2O_5 coatings with photothermal effect for bone tumor therapy. *Ceram Int*. 2018;44(11):12002–12006. Doi: https://doi.org/10.1016/j.ceramint.2018.03.155

View Article Online
DOI: 10.1039/D5CP01788B

46. Latas N, Pjević D, Rajić V, Ivanović M, Jugović D, Stojadinović S, Cvjetićanin N. Enhancing electrical and optical properties of anatase TiO_2 nanotubes through electrochemical lithiation. *J Alloys Compd*. 2024;1005:176081. Doi: https://doi.org/10.1016/j.jallcom.2024.176081

47. Abazović N, Čomor M, Dramićanin M, Jovanović D, Ahrenkiel S, Nedeljković J. Photoluminescence of anatase and rutile TiO_2 particles. *J Phys Chem B*. 2006;110:25366. Doi: https://doi.org/10.1021/jp064454f

48. Pan X, Yang MQ, Fu X, Zhang N, Xu YJ. Defective TiO_2 with oxygen vacancies: synthesis, properties, and photocatalytic applications. *Nanoscale*. 2013;5:3601. Doi: https://doi.org/10.1039/c3nr00476g

49. Zhang Z, Zhang L, Li W, Yu A, Wu P. Carbon-Coated Mesoporous TiO_2 Nanocrystals Grown on Graphene for Lithium-Ion Batteries. ACS Appl Mater Interfaces. 2015;7:10395–10400. Doi: https://doi.org/10.1021/acsami.5b01450

50. Jin J, Huang SZ, Li Y, Tian H, Wang HE, Yu Y, Chen LH, Hasan T, Su BL. Hierarchical nanosheet-constructed yolk–shell TiO_2 porous microspheres for lithium batteries with high capacity, superior rate and long cycle capability. Nanoscale. 2015;7:12979. Doi: https://doi.org/10.1039/C5NR02800K

51. Wang W, Sa Q, Chen J, Wang Y, Jung H, Yin Y. Porous TiO_2/C nanocomposite shells as a high-performance anode material for lithium-ion batteries. ACS Appl Mater Interfaces. 2013;5:6478–6483. Doi: https://doi.org/10.1021/am402350n

View Article Online
DOI: 10.1039/D5CP01788B

52. Latas N, Cvjetićanin N. Large Li-Ion Insertion Capacity of Thin-Wall Anatase TiO_2 Nanotubes at 25 °C–55 °C. J Electrochem Soc. 2023;170:090504. Doi: https://doi.org/10.1149/1945-7111/acf0e1

53. Jyothilakshmi S, Lee YS, Aravindan V. Subtractive synthesis of anatase TiO_2 nanostructures for sustained Li-storage in faradaic and non-faradaic assemblies. J Power Sources. 2025;652:237543. Doi: https://doi.org/10.1016/j.jpowsour.2025.237543

54. Wang JS, Liao GB, Chong Z, Ho CH, Huang PC, Huang JL, Chang CC, Sahu DR, Shen YM. Carbon-coated nonstoichiometric TiO_x for application of Li-ion battery anodes in fast charging—in situ XRD study. J Electroanal Chem. 2025;988:119127. Doi: https://doi.org/10.1016/j.jelechem.2025.119127

55. Levi MD, Aurbach D. Simultaneous measurements and modeling of the electrochemical impedance and the cyclic voltammetric characteristics of graphite electrodes doped with lithium. J Phys Chem B. 1997;101:4630–4640. Doi: https://doi.org/10.1021/jp9701909

View Article Online
DOI: 10.1039/D5CP01788B

Data Availability Statement

The data corresponding to Electrochemical tests is available in Supplementary material. Other data that support the findings of this study are available from the corresponding author upon reasonable request.